

Critical behavior of spherically symmetric domain wall collapse

Taishi Ikeda* and Chul-Moon Yoo†

*Departure of Physics, Graduate School of Science,
Nagoya University, Nagoya 464-6602, Japan*

Abstract

Critical collapse of a spherically symmetric domain wall is investigated. The domain wall is made of a minimally coupled scalar field with a double well potential. We consider a sequence of the initial data which describe a momentarily static domain wall characterized by its initial radius. The time evolution is performed by a full general relativistic numerical code for spherically symmetric systems. In this paper, we use the maximal slice gauge condition, in which spacelike time slices may penetrate the black hole horizon differently from other widely used procedures. In this paper, we consider two specific shapes of the double well potential, and observe the Type II critical behavior in both cases. The mass scaling, sub-critical curvature scaling, and those fine structures are confirmed. The index of the scaling behavior agrees with the massless scalar case.

arXiv:1610.07280v1 [gr-qc] 24 Oct 2016

*Electronic address: ikeda@gravity.phys.nagoya-u.ac.jp

†Electronic address: yoo@gravity.phys.nagoya-u.ac.jp

I. INTRODUCTION

Solutions for the Einstein equations and their non-linear dynamics have rich structure and behavior, and they have been extensively investigated in many aspects for a century. After numerical techniques were established, research on the non-linear dynamics has been developed a lot, and still continues to attract much attention up to the present date. The critical collapse, which was firstly observed by Choptuik [1] for the spherically symmetric massless scalar system with numerical simulation, is one of the most interesting discoveries in non-linear gravitational dynamics. After the Choptuik's discovery, many researchers have discovered the critical collapse in several systems such as axisymmetric gravitational wave collapse [2, 3], spherically symmetric gravitational collapse of a perfect fluid [4, 5] and collapse of collisionless matter particles [6].

Let us consider a collapsing system whose initial data are characterized by a parameter p , and suppose that a black hole is finally formed for the solutions with $p > p_*$ (supercritical), while it is not the case for $p < p_*$ (subcritical). The critical behavior can be observed near the threshold of the black hole formation $p \sim p_*$. It has some characteristic features of the intermediate state of the gravitational collapse and the behavior of the black hole mass in the supercritical region. The intermediate state of the gravitational collapse around the threshold does not depend on how to parametrize the initial data, and it is called a critical solution.

Here, we focus on the so-called Type II critical collapse associated with a discrete self-similar critical solution (see e.g., a review paper [7] for general cases). In this case, the black hole mass in the supercritical region obeys the scaling law with a periodic fine structure as follows: $\ln M_{\text{BH}} = \nu \ln |p - p_*| + c + f(\ln |p - p_*|)$, where c is a constant, and $f(x)$ is a periodic function satisfying $f(x + \varpi) = f(x)$. The index ν and period ϖ take universal values irrespective of the parametrization of the initial data. An example of this type is the spherically symmetric massless scalar system [1, 8], and we obtain $\nu \sim 0.377$ and $\varpi \sim 4.6$ in this case.

Scaling laws can be also observed not only in the super-critical region but also in the subcritical region for some physical quantities. Garfinkle reported the following scaling laws of the maximum values of the curvature invariants at the origin of a spherical system: $|R|_{\text{max}} \propto |p - p_*|^{-2\nu}$ and $|R_{\mu\nu}R^{\mu\nu}|_{\text{max}} \propto |p - p_*|^{-4\nu}$, where ν is the index of the black hole

mass scaling [9]. It has been revealed that such rich phenomena of the critical collapse is related to the structure of the phase space [10, 11]. Other related works are summarized in a review paper [7].

Finding universal phenomena in complicated non-linear dynamics is important and useful to understand characteristic features of the theory. The critical collapse may reflect a universal feature of gravitational theory. Investigation into the critical collapse may provide not only deep understanding of gravitational theory but also astrophysical implication. For instance, the threshold for the black hole formation is particularly important for the primordial black holes. Some of the primordial black holes would have been formed in the early universe as a result of near critical collapse. Therefore, the scaling behavior would be important and useful to predict the mass spectrum of the number density of the primordial black holes [12].

Choptuik discussed the critical collapse of the scalar field with a polynomial potential [13], and concluded that the polynomial potential is irrelevant under the critical collapse, because the kinetic term of the scalar field dominates under the discrete self-similar spacetime. That is, if the critical behavior is realized for the scalar field with a polynomial potential with a discrete self-similar spacetime as the intermediate state, it is expected that the scaling law is identical to the massless case. However, in general, it is nontrivial if the critical collapse with a discrete self-similar spacetime is actually realized or not with a polynomial potential. In fact, as is reported in Refs. [14, 15], the critical collapse of the massive scalar system can be different from the massless case depending on the relative value of the mass of the scalar field to the physical scale characterizing the initial data.

In this paper, we simulate spherically symmetric domain wall collapse of a scalar field with a double well potential. Dynamics of a spherically symmetric domain wall has been investigated in Ref. [16] on the flat background. It has been shown that a black hole can be formed by gravitational collapse of the domain wall in Ref. [17]. Astrophysical implication of the primordial black holes from domain wall collapse is discussed in Ref. [18]. Recently, it was reported that mass scaling appears in the domain wall collapse and the index of the scaling agrees with the index in the massless scalar system [19]. While, the fine structure has not been confirmed yet. As is noted above, depending on the value of the parameter for the potential, there is a possibility to obtain different behavior from the Type II critical behavior. Therefore, in this paper, we adopt different parameter sets from those in Ref. [19],

and discuss whether the mass scaling and the fine structure appear.

One remarkable feature of our work is in the gauge condition for time slices. In many papers about the critical collapse, the areal polar gauge condition or null coordinates are used. In the areal polar gauge, the black hole horizon is identified by the vanishing lapse function. Therefore, time slices cannot penetrate the black hole horizon. In the case of null coordinates, the apparent horizon is foliated by null surfaces starting from the outer-boundary in the asymptotic region. While, in our case, we get a foliation of spatial sections of the apparent horizon. There are a few papers in which a similar gauge condition to ours is used [6, 15, 20]. In these papers, and also in this paper, the black hole mass is defined by the half of the areal radius of the apparent horizon at the moment of the apparent horizon formation. Obviously, the definition of the black hole mass depends on the time slice. However, in spite of this fact, the critical behavior appears, as is reported in Refs. [6, 15, 20]. It should be noted that, the areal radius of the apparent horizon with a spatial section is, of course, different from the areal radius of the event horizon near the null infinity. Therefore, scaling behaviors of these two horizons should be independently discussed and compared with each other.

This paper is organized as follows. In the next section, we explain our formulation and numerical schemes. Initial data for the numerical simulation is shown in section III. In section IV, we provide our numerical results, and discuss the mass scaling, fine structure and curvature scaling. Section V is devoted to a summary and discussion.

Throughout this paper, we use the geometrized units in which the speed of light and Newton's gravitational constant are one, respectively.

II. FORMULATION AND NUMERICAL SCHEMES

A. Formulation

We consider the Einstein-scalar system with a double well potential whose Lagrangian is given by

$$S = \int d^4x \sqrt{-g} \left\{ \frac{R}{16\pi} - \frac{1}{2} \nabla_\mu \Phi \nabla^\mu \Phi - V(\Phi) \right\}, \quad (2.1)$$

where $g_{\mu\nu}$ is the metric tensor, R is the Ricci scalar and Φ is a scalar field. $V(\Phi)$ is the double well potential given by

$$V(\Phi) = \frac{\lambda}{24}(\Phi^2 - \sigma^2)^2, \quad (2.2)$$

where λ and σ are constant parameters. We focus on spherically symmetric spacetimes, whose line element is described by

$$ds^2 = -\alpha^2(t, r)dt^2 + \psi^4(t, r) \{ \gamma(t, r)^{-2}(dr + r\beta(t, r)dt)^2 + \gamma(t, r)r^2d\Omega^2 \}, \quad (2.3)$$

where $d\Omega^2$ is the solid angle element, and ψ , α , β and γ are independent functions of t and r . Under this ansatz, the 3-metric γ_{ij} is expressed as follows:

$$\gamma_{ij} = \psi^4 \text{diag}(\gamma^{-2}, \gamma r^2, \gamma r^2 \sin^2 \theta). \quad (2.4)$$

The extrinsic curvature K_{ij} of each time slice can be expressed by using the two independent components $K \equiv \gamma^{ij}K_{ij}$ and $A \equiv (K_{\theta\theta} - \frac{1}{3}K\gamma_{\theta\theta})/(\psi^4 r^2)$.

Substituting the metric form (2.3) into the Einstein equations and the equation of motion for the scalar field, we get the following time evolution equations:

$$(\partial_t - r\beta\partial_r)\psi = \frac{1}{6}\psi(3\beta + r\beta' - \alpha K), \quad (2.5)$$

$$(\partial_t - r\beta\partial_r)K = \alpha \left\{ \frac{1}{3}K^2 + 6\frac{A^2}{\gamma^2} + 8\pi\Pi^2 - 8\pi V(\Phi) \right\} - \psi^{-4}\gamma^2 \left\{ \Delta\alpha + 2\alpha' \left(\frac{\psi'}{\psi} + \frac{\gamma'}{\gamma} \right) \right\}, \quad (2.6)$$

$$(\partial_t - r\beta\partial_r)\gamma = -2\alpha A - \frac{2}{3}r\gamma\beta', \quad (2.7)$$

$$\begin{aligned} (\partial_t - r\beta\partial_r)A = & \alpha K A - 2\alpha\frac{A^2}{\gamma} - \frac{2}{3}rA\beta' + \psi^{-4} \left\{ -\frac{1}{6}\gamma^3(\Delta\alpha - 3\alpha'') - \frac{1}{3}\alpha\gamma^3 \left(\frac{\Delta\psi}{\psi} - 3\frac{\psi''}{\psi} \right) \right. \\ & - \frac{1}{6}\alpha(1 + \gamma)\Delta\gamma + \frac{1}{6}\alpha(1 + \gamma + \gamma^2)\gamma'' - \frac{1}{3}\alpha(1 + \gamma + \gamma^2) \left(-\frac{\gamma - 1}{r^2} + \frac{\gamma'}{r} \right) + \frac{1}{6}\alpha'\gamma^2\gamma' \\ & \left. - \frac{4}{3}\alpha'\gamma^3\frac{\psi'}{\psi} + \frac{1}{3}\alpha\gamma^2\gamma'\frac{\psi'}{\psi} - 2\alpha\gamma^3\frac{\psi'^2}{\psi^2} + \frac{8}{3}\pi\alpha\gamma^3\Phi'^2 \right\}, \end{aligned} \quad (2.8)$$

$$(\partial_t - r\beta\partial_r)\Phi = -\alpha\Pi, \quad (2.9)$$

$$(\partial_t - r\beta\partial_r)\Pi = \alpha\Pi K - \psi^{-4}\alpha\gamma^2 \left\{ \Delta\Phi + 2\Phi' \left(\frac{\gamma'}{\gamma} + \frac{\psi'}{\psi} + \frac{\alpha'}{2\alpha} \right) \right\} + \alpha V'(\Phi), \quad (2.10)$$

where Π is the conjugate momentum of Φ . The Hamiltonian constraint and the momentum constraint can be written as

$$\begin{aligned} \frac{\Delta\psi}{\psi} + \frac{1}{8} \left(5\frac{\Delta\gamma}{\gamma} - 3\frac{\gamma''}{\gamma} \right) + \pi\Phi'^2 + 2\pi\gamma^{-2}\psi^4 V(\Phi) + \frac{(\gamma^2 + \gamma + 1)(\gamma - 1)}{4\gamma^3 r^2} \\ + \frac{\gamma'}{\gamma} \left(2\frac{\psi'}{\psi} + \frac{3}{16}\frac{\gamma'}{\gamma} \right) + \frac{\psi^4}{\gamma^2} \left(\frac{3A^2}{4\gamma^2} + \pi\Pi^2 - \frac{1}{12}K^2 \right) = 0, \end{aligned} \quad (2.11)$$

$$A' + \frac{\gamma}{3}K' + 4\pi\gamma\Pi\Phi' + \frac{3A}{r} + \frac{A\gamma'}{2\gamma} + 6A\frac{\psi'}{\psi} = 0. \quad (2.12)$$

The boundary condition for the variables at the origin is imposed by the Neumann boundary condition in order to guarantee regularities. In addition, we require that γ and A satisfy the local flatness condition:

$$\gamma(t, r = 0) = 1, \quad A(t, r = 0) = 0. \quad (2.13)$$

The Neumann boundary condition and the local flatness condition regularize the $1/r$ and $1/r^2$ terms in Eq. (2.8) and constraint equations. It can be straightforwardly checked that, if the condition (2.13) is satisfied on the initial hypersurface and the time evolution equations are exactly satisfied, the condition (2.13) is kept for every time step. However, when the time evolution equations are numerically solved, the local flatness condition can be violated due to numerical errors. When the Neumann boundary condition for A and γ is imposed, the local flatness condition cannot be explicitly enforced. In consequence, numerical instability may be generated by $1/r$ and $1/r^2$ terms in the original evolution equation (2.8) for A . In order to avoid the numerical instability, instead of Eq. (2.8), we solve the momentum constraint (2.12) for A at each time step. At the origin, the equation (2.12) is evaluated by using the Neumann boundary condition and the local flatness condition (2.13).

While the appearance of $1/r$ and $1/r^2$ terms is avoided in the evolution equation by the prescription stated above, we still have those terms in the Hamiltonian constraint (2.11). Due to these terms, we suffer from the large cancellation error in evaluation of the constraint violation near the origin, and we cannot use the Hamiltonian constraint (2.11) to check the accuracy of the numerical computation. In order to overcome this difficulty, we introduce the auxiliary field $\Gamma(t, r)$ defined by

$$\Gamma \equiv \gamma' + \frac{3}{r}(\gamma - 1). \quad (2.14)$$

Then, the constraint equation (2.11) becomes

$$\begin{aligned} \frac{\Delta\psi}{\psi} + \frac{1}{8}\left(5\frac{\Delta\gamma}{\gamma} - 3\frac{\gamma''}{\gamma}\right) + \pi\Phi'^2 + 2\pi\gamma^{-2}\psi^4V(\Phi) + \frac{\gamma^2 + \gamma + 1}{8\gamma^3}\left(\Delta\gamma - \frac{1}{3}\gamma'' - \frac{2}{3}\Gamma'\right) \\ + \frac{\gamma'}{\gamma}\left(2\frac{\psi'}{\psi} + \frac{3}{16}\frac{\gamma'}{\gamma}\right) + \frac{\psi^4}{\gamma^2}\left(\frac{3A^2}{4\gamma^2} + \pi\Pi^2 - \frac{1}{12}K^2\right) = 0. \end{aligned} \quad (2.15)$$

From the time evolution equations, we can derive the evolution equation for Γ as follows:

$$\begin{aligned} (\partial_t - r\beta\partial_r)\Gamma = \alpha\frac{\gamma'}{\gamma}A + 8\pi\alpha\gamma\Pi\Phi' + 12\alpha A\frac{\psi'}{\psi} + \frac{2}{3}\alpha\gamma K' - 2\alpha'A - \frac{8}{3}\gamma\beta' \\ + \frac{1}{3}r\gamma'\beta' - \frac{2}{3}r\gamma\beta'' + \beta\Gamma. \end{aligned} \quad (2.16)$$

We check the violation of Eqs. (2.14) and (2.15) throughout the time evolution as measures of numerical accuracy.

The evolution equation for A , which we do not solve in this work, can be also derived from the evolution equation as follows:

$$\begin{aligned}
(\partial_t - r\beta\partial_r)A = & \alpha KA - 2\alpha\frac{A^2}{\gamma} - \frac{2}{3}rA\beta' + \psi^{-4} \left\{ -\frac{1}{6}\gamma^3(\Delta\alpha - 3\alpha'') - \frac{1}{3}\alpha\gamma^3\left(\frac{\Delta\psi}{\psi} - 3\frac{\psi''}{\psi}\right) \right. \\
& -\frac{1}{6}\alpha(1+\gamma)\Delta\gamma + \frac{1}{18}\alpha(1+\gamma+\gamma^2)\gamma'' + \frac{1}{9}\alpha(1+\gamma+\gamma^2)\Gamma' + \frac{1}{6}\alpha'\gamma^2\gamma' \\
& \left. -\frac{4}{3}\alpha'\gamma^3\frac{\psi'}{\psi} + \frac{1}{3}\alpha\gamma^2\gamma'\frac{\psi'}{\psi} - 2\alpha\gamma^3\frac{\psi'^2}{\psi^2} + \frac{8}{3}\pi\alpha\gamma^3\Phi^2 \right\}. \quad (2.17)
\end{aligned}$$

We note that, in this scheme, $1/r$ and $1/r^2$ terms are also removed from the time evolution equation (2.17)(see also Ref. [25]). It is also worth to note that this procedure is quite similar to the so-called BSSN scheme in numerical relativity [21, 22].

B. Gauge condition

For the shift vector, we simply set

$$\beta(t, r) = 0. \quad (2.18)$$

For the lapse function, we use the maximal slice condition $K = 0$. By this condition, the time evolution equation for K gives the elliptic partial differential equation for $\alpha(t, r)$:

$$\Delta\alpha + 2\alpha'\left(\frac{\psi'}{\psi} + \frac{\gamma'}{\gamma}\right) = \alpha\psi^4\gamma^{-2} \left\{ 6\frac{A^2}{\gamma^2} + 8\pi\Pi^2 - 8\pi V(\Phi) \right\}. \quad (2.19)$$

Because the solution for this equation has the ambiguity of a constant factor, we normalize it so that the lapse function may be unity at far boundary.

The lapse α is a non-trivial function of the radial coordinate, and it may have the value larger than unity for some cases. In such cases, we need to care about the Courant-Friedrichs-Lewy condition (CFL condition). In order to appropriately impose the CFL condition for the physical time scale, we normalized the time step interval Δt as $\alpha_{\max}\Delta t = 0.75\Delta$, where Δ is the grid interval of the radial coordinate and α_{\max} is the maximum value of the lapse function at each time step.

C. Numerical scheme

We implemented the equations (2.7), (2.9), (2.10), (2.12) and (2.19) in a numerical code. Because we use the maximal slice condition, the time derivative of ψ vanishes, and we do not need to solve the Eq. (2.5). The integration in time is performed by the iterative Crank-Nicolson scheme[23], and spatial derivatives are evaluated by using a 4th order finite difference method except for γ in $r < 0.01/\mu$, where spatial derivatives of γ is evaluated by using the 2nd order central difference method. The laplacian terms in each equation at the origin are evaluated by using the CARTOON method in $r < 0.01/\mu$ [24].

III. INITIAL DATA

Let us consider a momentarily static domain wall based on the isotropic coordinate \tilde{r} , for which a line element dh^2 on the initial hyper-surface can be expressed as

$$dh^2 = \tilde{\psi}^4 (d\tilde{r}^2 + \tilde{r}^2 d\Omega^2). \quad (3.1)$$

The relation between the coordinate r and \tilde{r} will be given later. From the momentarily static condition, K , A and Π are assumed to be zero at $t = 0$. Consequently, the momentum constraint is trivially satisfied.

The initial scalar field profile is assumed to be the following form:

$$\Phi|_{t=0} = \sigma \tanh\left(\frac{\tilde{r} - r_0}{l}\right) + \sigma \left\{ -1 - \tanh\left(\frac{\tilde{r} - r_0}{l}\right) \right\} \exp\left\{ -\left(\frac{\tilde{r}}{l}\right)^4 \right\}, \quad (3.2)$$

where r_0 is the initial radius of the domain wall and l is the width of the domain wall. The width l is given by the value of the planar domain wall solution as $l = \frac{2}{\sigma} \sqrt{\frac{3}{\lambda}} \equiv \sqrt{\frac{2}{\mu^2}}$ (see Fig1). The first term locally describes the planar domain wall solution for large \tilde{r} . While the second term is introduced to regularize the scalar field at the origin.

Because it is expected that curvature values for near critical cases are very large, high numerical resolution is needed especially in the central region to resolve the critical behavior. In order to realize the finer resolution near the origin, we use the coordinate r which is related to the isotropic coordinate \tilde{r} as follows:

$$r = \begin{cases} \tilde{r} & (0 < \tilde{r} < R), \\ \tilde{r} + \left(\frac{\tilde{r}-R}{w}\right)^\rho & (R < \tilde{r}), \end{cases} \quad (3.3)$$

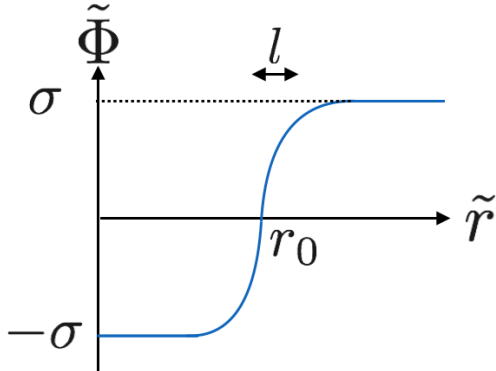


FIG. 1: The profile of the scalar field for the initial data.

where R , w and ρ are constant parameters. Performing the coordinate transformation from \tilde{r} to r , γ can be read off from the spatial part of the metric (2.3). Γ can be also calculated by the definition (2.14). Then, solving the Hamiltonian constraint equation (2.11) for ψ , we can obtain the initial data set.

It is worthy to note that, by virtue of the new coordinate r , the physical distance to the outer numerical boundary can be so large that the scalar waves cannot reach the outer boundary. Therefore, during the time evolution, the asymptotically flat boundary condition can be easily implemented for the radial coordinate r .

IV. RESULTS

A. Setup

Hereafter we express all the variables in the unit of μ . The radius of the domain wall r_0 is the only parameter which characterizes the initial data of this system. We have another parameter λ to specify the potential shape. In Ref. [19], the cases $\lambda = 30000\mu^2$ and $\lambda = 60000\mu^2$ are investigated. We consider smaller values of λ/μ^2 and higher potential barrier between the potential minima than the cases in Ref. [19], so that we can observe characteristic behavior due to existence of the two potential minima. In this paper, we investigate the cases $\lambda = 1000\mu^2$ and $\lambda = 2000\mu^2$. As for the parameters in the coordinate transformation (3.3), we use the following two parameter sets:

$$\text{Param - 1 : } R = 0.1/\mu, w = 0.05/\mu, \rho = 6 \text{ for } 0 < r < 0.2, \quad (4.1)$$

$$\text{Param - 2 : } R = 0.03/\mu, w = 0.01/\mu, \rho = 6 \text{ for } 0 < r < 0.05. \quad (4.2)$$

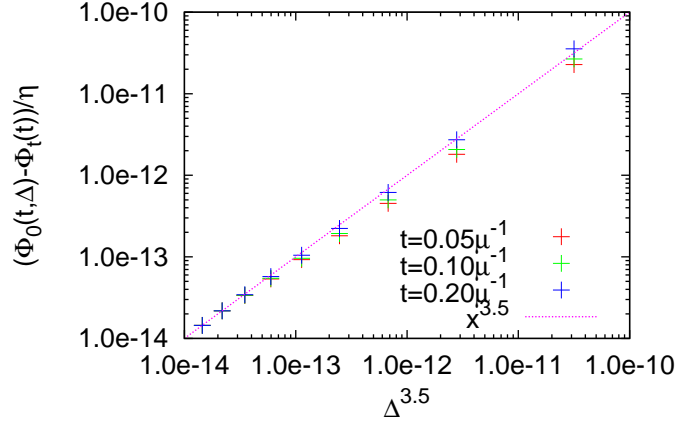


FIG. 2: The convergence of $\Phi_0(t, \Delta)$ for each time step.

In both cases, the maximum value of the areal radius is about $60/\mu$.

B. Convergence test

Before showing main results, in this subsection, we present the result of a convergence test for our numerical code by using simulation with $r_0 = 0$ for each resolution. We show the result for $\lambda = 2000\mu^2$. For simplicity, we focus on the value $\Phi_0(t, \Delta) := \Phi(t, r = 0; \Delta)$, where we have explicitly written the dependence on the grid interval Δ . If our numerical code obeys the n -th order convergence, we obtain

$$\Phi_0(t, \Delta) = \Phi_t(t) + \eta\Delta^n, \quad (4.3)$$

where $\Phi_t(t) := \lim_{\Delta \rightarrow 0} \Phi_0(t, \Delta)$ is the true value for the infinite resolution and η is a constant. Since a 2nd order finite difference method is partially used in our numerical code, we expect at least the 2nd order convergence to our numerical code, that is $n \geq 2$. As is shown in Fig. 2, the value of n can be read off as $n \sim 3.5$ from our numerical results, and $\Phi_t(t)$ and η can be evaluated by using the least square fitting assuming $n = 3.5$.

C. Threshold

First, we summarize our parameter setting for each value of the initial radius r_0 of the domain wall in Table I. For $\lambda = 1000\mu^2$ and $\lambda = 2000\mu^2$ cases, the thresholds r_* of the BH

$$\lambda = 1000\mu^2$$

Sub/Super critical	Initial domain wall radius [μ^{-1}]	Grid interval [μ^{-1}]	Param-1/2
Super	2.500000000 \sim 1.455625000	5.0×10^{-5}	Param-1
Super	1.455624950 \sim 1.455624600	2.5×10^{-5}	Param-1
Super	1.455624500 \sim 1.455624350	1.0×10^{-6}	Param-2
Sub	1.455624200 \sim 1.455624000	1.0×10^{-6}	Param-2
Sub	1.455623500 \sim 1.440000000	5.0×10^{-5}	Param-1

$$\lambda = 2000\mu^2$$

Sub/Super critical	Initial domain wall radius [μ^{-1}]	Grid interval [μ^{-1}]	Param-1/2
Super	4.200000000 \sim 2.216000000	5.0×10^{-5}	Param-1
Super	2.206000000 \sim 2.199162000	5.0×10^{-5}	Param-1
Terminated	2.215000000 \sim 2.207000000	Terminated	
Super	2.199160000 \sim 2.199078380	2.0×10^{-5}	Param-1
Super	2.199078377 \sim 2.199078367	5.0×10^{-6}	Param-2
Sub	2.199078332 \sim 2.199077000	5.0×10^{-6}	Param-2
Sub	2.199076000 \sim 2.199010000	2.5×10^{-5}	Param-1
Sub	2.199000000 \sim 2.194000000	5.0×10^{-5}	Param-1

TABLE I: Table of the parameter region of our numerical simulation and the grid interval for each simulation. The leftmost column shows whether the parameter is in the super critical region or the subcritical region.

formation are given by $1.4556243366/\mu$ and $2.199078357/\mu$, respectively.

In the $\lambda = 2000\mu^2$ case, there is the parameter region in which the lapse function diverges at the origin during the time evolution. This behavior might suggest that the time slice condition is not appropriate for this parameter region. However, the value of r_0 in this region is far from the threshold value, and it is not a matter to investigate the critical behavior.

Apart from the parameter region where the calculation is terminated, we do not observe the discrete change of the black hole formation time, and non trivial phase transition such as the phase transition between the delayed collapse phase and the prompt collapse phase

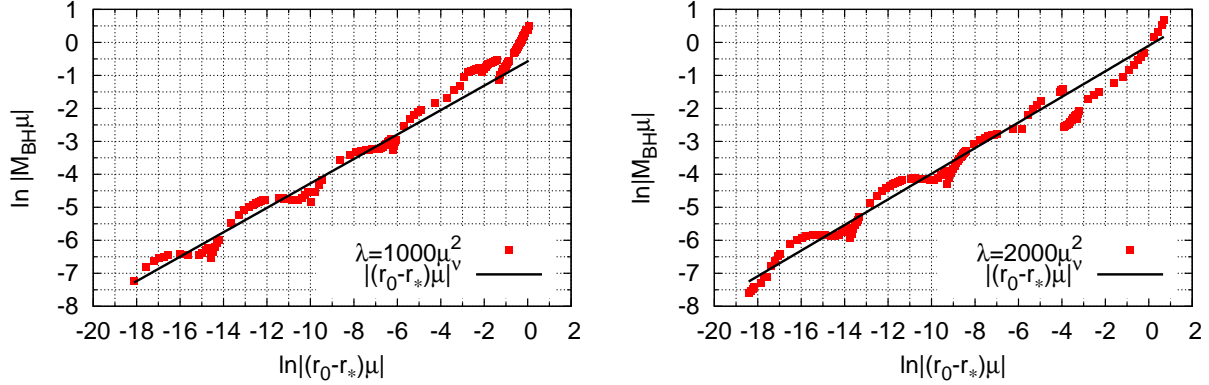


FIG. 3: The left panel shows the mass scaling for the $\lambda = 1000\mu^2$ case, and the right panel shows the mass scaling for the $\lambda = 2000\mu^2$ case. In each panel, the dots denote the numerical results, and the line denotes the fitting function $M_{\text{BH}} = \zeta |(r_0 - r_*)\mu|^\nu$. We determined the coefficient ζ and ν by using the least squares fitting in the region $\ln |(r_0 - r_*)\mu| < -5$. As a result, for $\lambda = 1000\mu^2$, $\zeta \simeq 0.564$, $\nu \simeq 0.370$ and for $\lambda = 2000\mu^2$, $\zeta \simeq 0.905$, $\nu \simeq 0.388$.

reported in the massive scalar field case [15].

D. Mass scaling and the fine structure

We define the black hole mass M_{BH} as the half of the apparent horizon radius at the moment of the apparent horizon formation. In the supercritical region ($r_0 > r_*$), we can see the mass scaling around the threshold of the black hole formation (see Fig.3). As we can see in Fig. 3, the indices of the scaling agree with the index of the massless scalar system.

We can also see the fine structure in Fig. 3. In order to see the fine structure more clearly, we show the difference between M_{BH} and the scaling relation $\zeta |(r_0 - r_*)\mu|^\nu$ in Fig. 4. The periodic behaviors appear in the region $\ln |(r_0 - r_*)\mu| \lesssim -9$. The periods are about 4.5 in the log scale, which is close to the massless scalar case.

E. Mass discontinuity

There are some discontinuities in the behavior of the mass as a function of r_0 ($\ln |(r_0 - r_*)\mu| \simeq -10, -14.5$ for $\lambda = 1000\mu^2$, and $\ln |(r_0 - r_*)\mu| \simeq -9.5, -14.0$ for $\lambda = 2000\mu^2$).

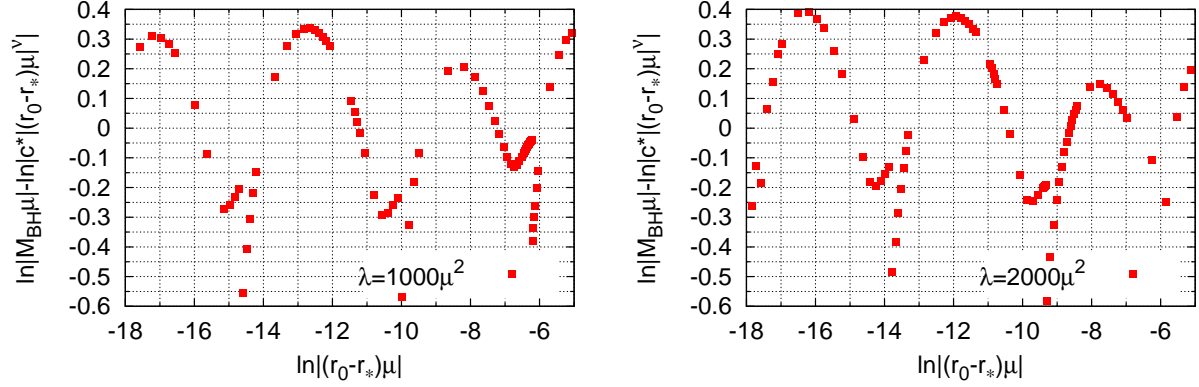


FIG. 4: The difference between M_{BH} and the scaling relation $\zeta|(r_0 - r_*)\mu|^\nu$. The left panel shows the case $\lambda = 1000\mu^2$, and the right panel shows the case $\lambda = 2000\mu^2$. The periodic behaviors appear in $\ln|(r_0 - r_*)\mu| \lesssim -9$. The periods are about 4.5 in the log scale.

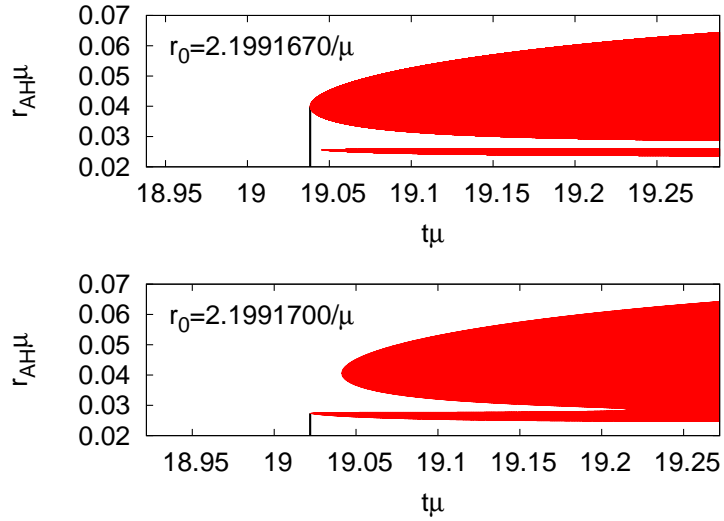


FIG. 5: Time evolution of the trapped region and marginally outer-trapped surfaces. The upper panel shows the case $r_0 = 2.1991670/\mu$ and, the lower panel shows the case $r_0 = 2.1991700/\mu$. The vertical line on the each graph corresponds to the moment of the apparent horizon formation.

The reason for this behavior can be understood by looking at the time evolution of the marginally outer-trapped surfaces, whose outgoing null expansion vanishes. We depict the time evolution of the trapped region and the marginally outer trapped surfaces in Fig. 5. In Fig. 5, the trapped region is described by the shaded region. In some period of time,

the trapped region is divided into two disconnected thick spherical shell regions. Therefore, we have two connected sequences of outer boundaries of the connected trapped regions. Consequently, the mass of the black hole at the moment of the horizon formation depends on which sequence appears first. The discrete transition of the black hole mass may happen at the parameter for which two sequences simultaneously appear. Since the multiple connected trapped regions are essential for this phenomenon, it cannot be realized in calculations with the areal polar gauge or the null coordinates. Similar behavior is also reported for the massless scalar system with a horizon penetrating gauge condition[20].

F. Scaling in the subcritical region

Let us consider the scaling behavior in the subcritical parameter region. We calculate the maximum absolute value of the curvature R and $R_{\mu\nu}R^{\mu\nu}$ at the origin in the subcritical parameter region ($r_0 < r_*$), which are denoted as $|R|_{\max}$ and $|R_{\mu\nu}R^{\mu\nu}|_{\max}$, respectively. As is mentioned in the introduction, it is expected that these curvatures also obey scaling laws. Because the behaviors of these curvatures are almost same as each other, only the relation between $|R|_{\max}$ and the initial radius of the domain wall is depicted in Fig. 6. As is shown in Fig.6, the behavior of the maximum value of the curvature agrees with the massless case. This is the expected result because, if the system comes to be governed by the scaling properties, the kinetic energy of the scalar field dominates and the potential term becomes less effective near the critical point [13].

As is also expected from the above consideration, we observe the scaling of the absolute maximum value of the conjugate momentum $|\Pi|_{\max}$ at the origin in the subcritical region (see Fig. 7). The index is expected from the dimensional analysis[10], because the dimension of the conjugate momentum of the scalar field is the inverse of the length scale. We can find that the sign of Π at the maximum absolute value synchronizes with the period of the fine structure. It visualizes that there is relation between the oscillation of the scalar field near the origin and the period of the fine structure in the parameter space.

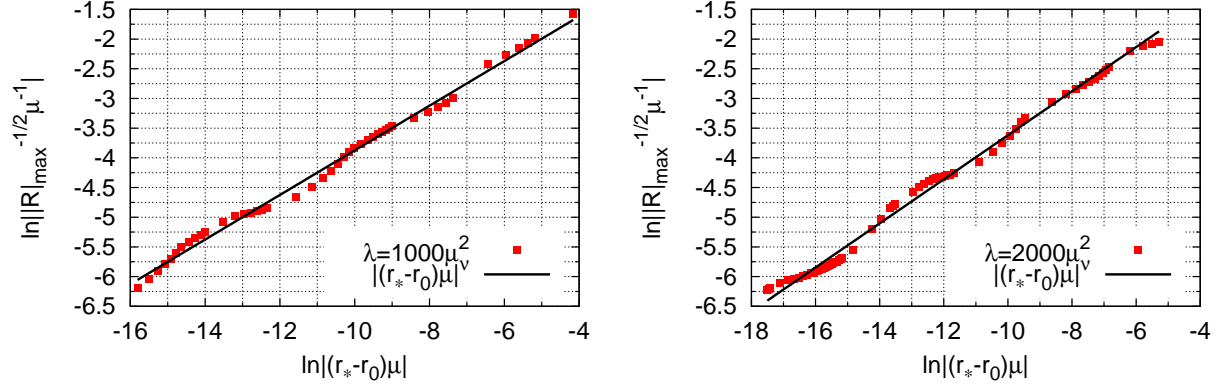


FIG. 6: The relation between the maximum value of the curvature and the initial radius of the domain wall. We plot $|R|_{\max}^{-1/2}$ as a function of $|(r_* - r_0)\mu|$. The left panel shows the case $\lambda = 1000\mu^2$, and the right panel shows the case $\lambda = 2000\mu^2$. The black line denotes the fitting function $\zeta|(r_* - r_0)\mu|^\nu$. The coefficient is determined by the least squares fitting in the region $\ln|(r_* - r_0)\mu| < -5$. As a result, we obtain $\nu \simeq 0.376$ for $\lambda = 1000\mu^2$, and $\nu \simeq 0.371$ for $\lambda = 2000\mu^2$.

V. SUMMARY AND DISCUSSION

In this paper, we have focused on the spherically symmetric minimally coupled scalar field system with a double well potential, and investigated gravitational collapse of a spherically symmetric domain wall. We have performed full general relativistic numerical simulation for two specific cases which have different parameter sets from the previous work[19]. As a result, the Choptuik's scaling and the fine structure have been confirmed. We have found that the index of the scaling and the period of the fine structure are close to the massless scalar case. Furthermore, for the subcritical region, we have checked that the maximum value of the curvature at the origin also obeys the scaling law with a similar index to the massless scalar case.

We have shown that the behavior of the black hole mass as a function of the initial radius of the domain wall is not necessarily smooth. Due to the non-trivial structure of the trapped region, the behavior of the black hole mass may have discontinuity. This behavior is peculiar in the analysis with spacelike horizon penetrating time slices. The origin of this discontinuity is the appearance of multiple connected trapped regions. Recently, similar

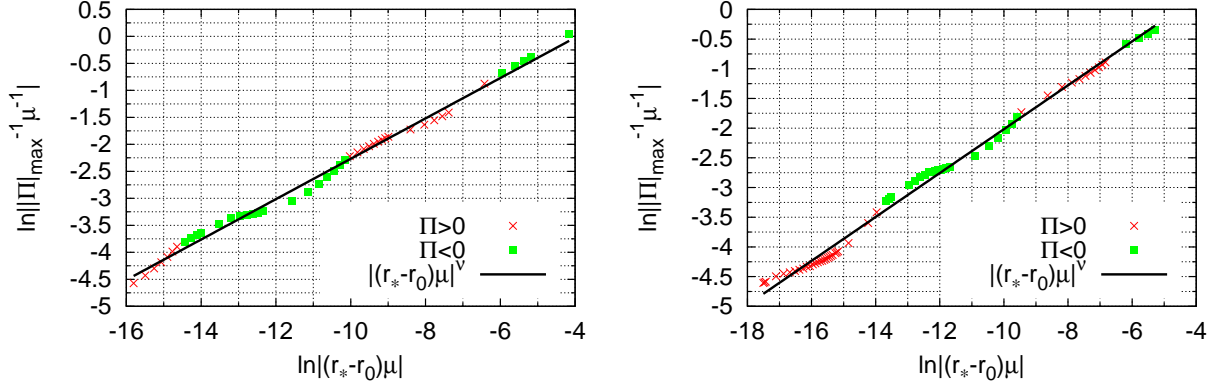


FIG. 7: The relation between the absolute maximum value of the conjugate momentum of the scalar field and the initial radius of the domain wall. The left panel shows the case $\lambda = 1000\mu^2$, and the right panel shows the case $\lambda = 2000\mu^2$. We plot $|\Pi|_{\max}$ as a function of $|(r_* - r_0)\mu|$. Each red(green) point corresponds to a case in which the maximum absolute value is realized by a positive (negative) value of the conjugate momentum. We can fit $|\Pi|_{\max}$ by the function $\zeta|(r_* - r_0)\mu|^{-\nu}$ (black line). By using the least squares fitting, ν is given by 0.374 for $\lambda = 1000\mu^2$, and 0.370 for $\lambda = 2000\mu^2$.

behavior is reported in Ref. [20]. They found that a new outer horizon appears after an apparent horizon initially appears, and the difference between the old apparent horizon and the new apparent horizon also obeys the scaling law. It may be interesting to check if the same scaling law can be realized with a non-trivial potential and discuss their differences. We leave it as a future work.

In this paper, the analyses have been done for two specific values of the parameter contained in the scalar field potential. In the supercritical region, when the initial radius of the domain wall changes, the black hole formation time changes smoothly. In this sense, non-trivial phase transition, such as the transition between the prompt collapse phase and the delayed collapse phase reported in the massive scalar system [15], has not been found. Apparently, we need further parameter search to complete the phase diagram of the spherical domain wall collapse as in the case of the massive scalar field [15].

VI. ACKNOWLEDGEMENTS

We would like to thank Hirotada Okawa, Tomohiro Harada, Rong-Gen Cai and Kazuhisa Okamoto for helpful discussion. This work was supported by JSPS KAKENHI Grant Numbers JP16K17688, JP16H01097(C.Y.).

-
- [1] M. W. Choptuik, *Phys. Rev. Lett.* **70**, 9 (1993).
 - [2] A. M. Abrahams and C. R. Evans, *Phys. Rev. Lett.* **70**, 2980 (1993).
 - [3] E. Sorkin, *Class. Quant. Grav.* **28**, 025011 (2011) [arXiv:1008.3319 [gr-qc]].
 - [4] C. R. Evans and J. S. Coleman, *Phys. Rev. Lett.* **72**, 1782 (1994) [gr-qc/9402041].
 - [5] D. Maison, *Phys. Lett. B* **366**, 82 (1996) [gr-qc/9504008].
 - [6] I. Olabarrieta and M. W. Choptuik, *Phys. Rev. D* **65**, 024007 (2002) [gr-qc/0107076].
 - [7] C. Gundlach and J. M. Martin-Garcia, *Living Rev. Rel.* **10**, 5 (2007) [arXiv:0711.4620 [gr-qc]].
 - [8] S. Hod and T. Piran, *Phys. Rev. D* **55**, 440 (1997) [gr-qc/9606087].
 - [9] D. Garfinkle and G. C. Duncan, *Phys. Rev. D* **58**, 064024 (1998) [gr-qc/9802061].
 - [10] T. Koike, T. Hara and S. Adachi, *Phys. Rev. Lett.* **74**, 5170 (1995) [gr-qc/9503007].
 - [11] C. Gundlach, *Phys. Rev. D* **55**, 695 (1997) [gr-qc/9604019].
 - [12] J. C. Niemeyer and K. Jedamzik, *Phys. Rev. Lett.* **80**, 5481 (1998) [astro-ph/9709072].
 - [13] M. W. Choptuik, *NATO Sci. Ser. B* **332**, 155 (1994).
 - [14] P. R. Brady, C. M. Chambers and S. M. C. V. Goncalves, *Phys. Rev. D* **56**, R6057 (1997) [gr-qc/9709014].
 - [15] H. Okawa, V. Cardoso and P. Pani, *Phys. Rev. D* **89**, no. 4, 041502 (2014) [arXiv:1311.1235 [gr-qc]].
 - [16] L. M. Widrow, *Phys. Rev. D* **40**, 1002 (1989).
 - [17] D. Garfinkle and R. Zbikowski, *Class. Quant. Grav.* **29**, 095015 (2012) [arXiv:1201.1491 [gr-qc]].
 - [18] S. G. Rubin, M. Y. Khlopov and A. S. Sakharov, *Grav. Cosmol. S* **6**, 51 (2000) [hep-ph/0005271].
 - [19] K. Clough and E. A. Lim, arXiv:1602.02568 [gr-qc].
 - [20] Z. Cao, R. G. Cai and R. Q. Yang, arXiv:1604.03363 [gr-qc].

- [21] M. Shibata and T. Nakamura, *Phys. Rev. D* **52**, 5428 (1995).
- [22] T. W. Baumgarte and S. L. Shapiro, *Phys. Rev. D* **59**, 024007 (1999) [gr-qc/9810065].
- [23] S. A. Teukolsky, *Phys. Rev. D* **61**, 087501 (2000) [gr-qc/9909026].
- [24] M. Alcubierre, S. Brandt, B. Bruegmann, D. Holz, E. Seidel, R. Takahashi and J. Thornburg, *Int. J. Mod. Phys. D* **10**, 273 (2001) [gr-qc/9908012].
- [25] M. Alcubierre and J. A. Gonzalez, *Comput. Phys. Commun.* **167**, 76 (2005) [gr-qc/0401113].